





Dark spots on Mercury show no signs of weathering during 30 Earth months

Yichen Wang ^{1,4}, Zhiyong Xiao ^{1,2,4}✉, Rui Xu ¹, Zhouxuan Xiao ³ & Jun Cui^{1,2}

Dark spots on Mercury are recently-formed thin and low-reflectance materials that are related with volatile activity and supposed to be much shorter-lived than their central hollows. Containing unique information about the possible building blocks of Mercury, dark spots have unresolved darkening phases, formation mechanism, and lifetime. Here we investigated reflectance spectra, sub-resolution roughness, and temporal changes of dark spots using the full-mission dataset of MESSENGER. We find that dark spots have the highest concentration of graphite and an intense outgassing origin. Temporal imaging for dark spots reveals no detectable reflectance changes in 30 Earth months, and possibly over 40 Earth years. These observations demonstrate that thermally unstable sulfides such as MgS and CaS are not the major components in dark spots. Possible reflectance changes of dark spots may occur at much longer time scales, providing a reference for modeling the spectral behavior of graphite caused by space weathering on Mercury.

¹ Planetary Environmental and Astrobiological Research Laboratory, School of Atmospheric Sciences, Sun Yat-sen University, Zhuhai, China. ² CAS Center for Excellence in Comparative Planetary, Hefei, China. ³ School of Geospatial Engineering and Science, Sun Yat-sen University, Zhuhai, China. ⁴ These authors contributed equally: Yichen Wang, Zhiyong Xiao. ✉email: xiaozhiyong@mail.sysu.edu.cn

Featuring unexpectedly low contents of Fe (1–2 wt%¹) and Ti (<0.8 wt%²) but surprisingly high contents of S (up to 4 wt%^{3,4}), C (up to 4 wt%^{5,6}) and Cl (up to 0.2 wt%⁷), the low-albedo planet Mercury has a more reduced⁸ and volatile-rich³ environment than the other terrestrial planets and the Moon. The identity and content of opaque facies and volatiles in non-polar regions of Mercury are key information to resolve its origin, as the high volatile content indicates that the inner-most planet might be formed at a much larger distance from the Sun and then migrated to its current position in the early Solar System⁹.

Landforms formed by volatile-involved geological processes, such as pyroclastic deposits dispersed by explosive volcanism¹⁰ and hollows dented by loss of subsurface volatiles¹¹, are widespread across Mercury. A consensus is emerged recently that carbon in the form of graphite may be the major opaque phase on Mercury¹², which was likely originated from the differentiation of a hypothesized mercurian magma ocean¹³. Destabilization of graphite in the harsh surface environment of Mercury might have supported the formation of hollows^{14,15}, and assimilation of sulfur and/or carbon from crustal rocks by ascending magma may have driven the explosive volcanism^{3,16–18}. Alternatively, other volatile species, such as chlorides¹⁹ and sulfides^{20–22}, were also proposed to be hollow-forming materials. The debating interpretations of hollow-forming materials (e.g., graphite, chlorides and sulfides) were all largely based on a rather weak absorption feature at the wavelength of ca. 600 nm^{14,19,21}, but earlier spectral sampling sites usually mixed different facies of hollow materials (i.e., bright halos, hollow floors, background host), which likely have experienced different degrees of devolatilization^{15,23}.

Dark spots are low-reflectance and diffuse materials developed outside of bright halos of hollows²⁴, and they are a key agent to inspect the possible relationship between graphite and hollow-forming volatiles on Mercury. Featuring young stratigraphic ages (less than ~270 Ma²⁴) and low reflectances, dark spots were interpreted to be dispersed by energetic outgassing, and the resultant ground cavities were subsequently used by the growth of hollows²³. Seeing in meter-scale high-resolution images, only one impact crater has been observed in flat floors of bright-haloed hollows, suggesting that many hollows may form in the past 0.1 million years¹⁵. Moreover, only a small portion of hollows were accompanied by dark spots, indicating that dark spot materials might have a much shorter lifetime than their central hollows, or some hollows might form without dark spots²⁴. A preliminary survey of reflectance spectra suggested that sulfides (e.g., MgS and CaS) may be the major component and also darkening phase in dark spots²⁴, but this interpretation is not consistent with the high reflectance of these sulfides¹².

The MErcury Surface, Space ENvironment, GEochemistry, and Ranging (MESSENGER) mission²⁵ provided multiple views of Mercury during the four-years orbital operation (from 18 March 2011 to 30 April 2015). Imagery data obtained during the entire mission of MESSENGER are now re-calibrated and released²⁶, permitting a systematic update for basic characteristics of dark spots, especially their potential short-term changes. Here we investigate the composition (especially the darkening phase) and evolution of dark spots using the entire imagery dataset obtained by MESSENGER.

Results

An updated global inventory of dark spots. We updated the global inventory of dark spots on Mercury (see Methods), yielding fifty-nine cases (Fig. 1a–b; Supplementary Table 1). Some of these were not confirmed previously (Fig. 1c–e) due to the limited dataset available in 2012. Dark spots are not preferentially distributed at the longitudes 0° and 180° (Fig. 1a), the two longitudinal poles that

receive more solar heating than the global average due to the spin-orbit resonance and the elliptical orbit of Mercury²⁷. Most (83%) dark spot materials belong to low-reflectance materials²⁸ (LRM; Fig. 1b) according to the spectral definition of LRM²⁹ (see Methods). Some dark spots have smaller areas than the resolution (665 m/pixel) of the global LRM map, and they are confirmed based on their isolated occurrences, diffuse morphology, and central hollows (e.g., Supplementary Fig. 1). Dark spots have been observed in terrains that have higher reflectance than low-reflectance materials²⁴ (e.g., low-reflectance blue plains²⁸; LBP). However, most (61%) dark spots are developed in LRM that features positive absorption depths at 600 nm (BD600; Fig. 1b), a spectral parameter¹² (see Methods) that may be proportionally correlated with graphite content^{6,29}. Compared to the background LRM, the diffuse dark spot materials exhibit lower reflectance and larger BD600 values (Fig. 1h, k).

Reflectance spectra of dark spots. By comparing the reflectance spectra for seven comparably large dark spots (each larger than 5 km²; Supplementary Fig. 2), typical LRM, and LBP, we confirm that dark spots have the lowest reflectance on Mercury (Fig. 2; ref. 24). Despite the small sizes of dark spots, the spectral sampling site for each case contained 2 to 6 pixels (665 m/pixel) to increase statistical significance. Supplementary Fig. 2 shows the locations of sampled pixels on co-registered high-resolution Narrow Angle Camera (NAC) images. The reflectance spectra of all the dark spots exhibit two shallow kinks at 560 and 750 nm (Fig. 2). The former feature was interpreted to be caused by graphite^{12,29}, sulfides²¹, or chlorites¹⁹. The spectral kink at ca. 750 nm was interpreted to be caused by pyroxenes that contain transitional elements such as Ti, Cr, Ni^{30,31}. This feature occurs in all mercurian materials but with different absorption depths, and it is not particularly related with dark spots or hollow-forming materials^{15,30}. As manifested by BD600 values (Supplementary Fig. 3), dark spot materials exhibit much larger band depths at 560 nm than both LRM and LBP (Fig. 2), in contrast to negative BD600 values for hollow floor materials (Supplementary Fig. 3; ref. 15).

Sub-pixel texture of dark spot materials. We surveyed suitable MESSENGER data for performing phase-ratio analyses for all dark spots (see Methods). In our analyses, larger-phase ratios correspond to steeper phase functions due to more pronounced shadow-hiding at sub-pixel scales, which are caused by a combination of a rougher surface and/or larger particle sizes³². From high-phase to low-phase observations, reflectances of all the investigated dark spots increased more significantly than those of the background regolith, followed by those of hollow halos (Fig. 3; Supplementary Tables 3–5). Hollow floors in the Eminescu crater are large enough to be resolvable by available phase-ratio images (Fig. 3i; ref. 33), and their reflectances increased less significantly than dark spots from high-phase to low-phase observations (Supplementary Table 5). Therefore, dark spot materials exhibit rougher textures (i.e., coarser grains and/or rougher surfaces) than both bright halos of hollow³³ and background regolith, but smoother than the collapsed lag deposits on flat hollow floors¹⁵. In addition, we noticed that dark spot materials closer to the central hollows, which were thicker than those further away²⁴ exhibit rougher sub-pixel textures (Fig. 3c; Supplementary Table 3), consistent with coarser grains being deposited closer to the central hollows.

Temporal changes of dark spot materials in 30 Earth months and longer periods. MESSENGER performed repeated observation for regions of interest during orbital operation²⁶. Owing to the small sizes of dark spots, we could analyze 3 cases (e.g., Fig. 4; Supplementary Figs. 4 and 5), which were covered by suitable

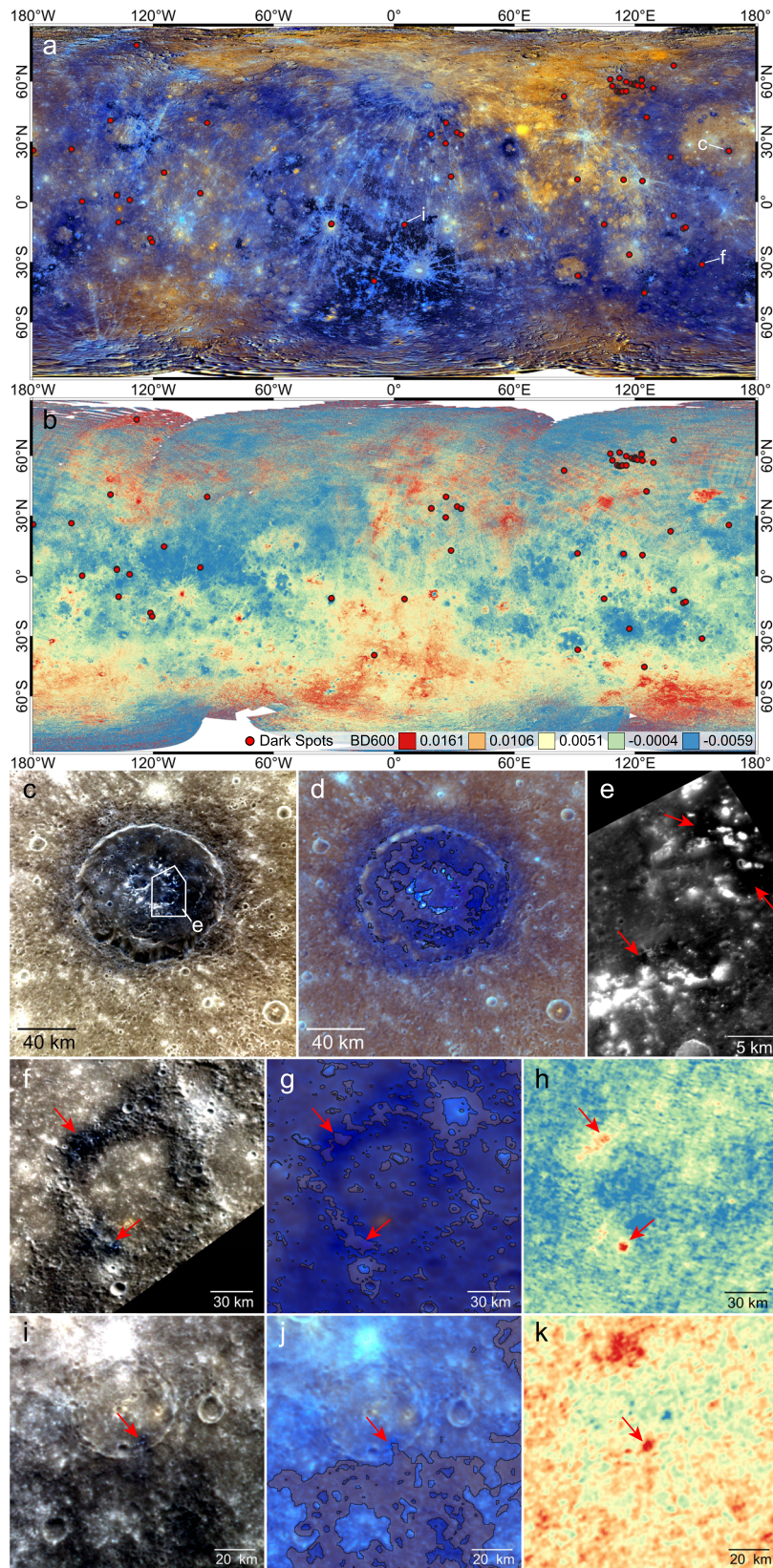


Fig. 1 Occurrence of dark spots on Mercury and their relationship with LRM. **a** The global distribution of dark spots (red dots) and LRM²⁹ (black shades) on Mercury. **b** Most dark spots occur in areas with positive BD600 values that is correlated with graphite contents (see Methods). **c** Dark spots in the Atget crater (166.38 °E, 25.57 °N) that were not confirmed previously²⁴. **d** LRM (translucent brown shades) is widespread in the peak ring of Atget crater. **e** A detailed view of dark spots in the peak ring (red arrows) with the lowest reflectance. Dark spots occur in regions that have higher positive BD600 values than the surrounding LRM (translucent brown shades) and other background units. **f-h** Two dark spots (red arrows) on the rim of an unnamed crater (154 °E, 30 °S). **i-k** Dark spot (red arrow) located at 5.24 °E, 11.42 °S. Panels **h** and **k** are in the same stretch with **b**. Base images used in all the panels are listed in the Supplementary Table 2 and provided by National Aeronautics and Space Administration (NASA).

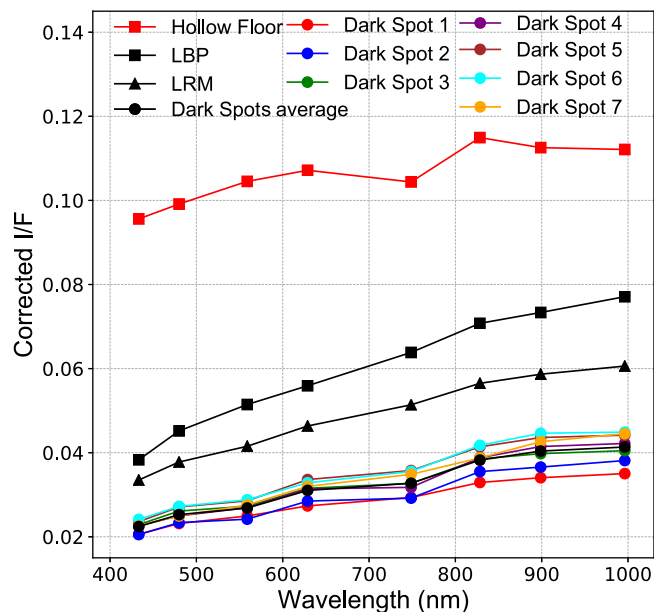


Fig. 2 Reflectance spectra of dark spots and their comparisons with those of hollow floors¹⁵, LRM⁵⁴, and LBP⁵⁴ on Mercury. Black dots are the average reflectance spectra of the seven dark spots.

high-resolution images for analyzing possible temporal changes (see Methods). The Kuiper crater (central coordinates 31.4 °W, 11.3 °S) is a comparably young crater ($\sim 280 \pm 60$ Ma³⁴) that features obvious impact rays and high-reflectance floors (Fig. 4a). Two dark spots developed in the crater floor (Fig. 4b) were imaged for four times at similar pixel scales and observation geometries, separated by 30 Earth months, i.e., the longest among all dark spots. In the co-registered NAC images (see Methods), we compared potential reflectance changes for the two dark spots and background crater floor (Fig. 4). Compared to the initial observation (T0; Fig. 4b), the average reflectance of dark spot 1 (DS1) changed from 0.117 (one standard deviation $\sigma = 0.0026$) to 0.118 ($\sigma = 0.0025$), 0.120 ($\sigma = 0.0024$), and back to 0.118 ($\sigma = 0.0024$) after 9 (Fig. 4d), 15 (Fig. 4e) and 30 Earth months (Fig. 4f), respectively (Fig. 4c; Supplementary Table 6). The corresponding reflectance ratios compared to the initial observation are 1.009, 1.026, and 1.009, respectively (Fig. 4g–i). The average reflectance of dark spot 2 (DS2) changed from 0.113 ($\sigma = 0.0020$) to 0.114 ($\sigma = 0.0027$), 0.116 ($\sigma = 0.0028$), and then back to 0.113 ($\sigma = 0.0027$); and that of the background crater floor materials changed from 0.123 ($\sigma = 0.0031$) to 0.124 ($\sigma = 0.0032$), 0.127 ($\sigma = 0.0029$), and then back to 0.124 ($\sigma = 0.0029$). In terms of reflectance ratios, DS1, DS2 and the background crater floor have identical behavior (Fig. 4g–i; Supplementary Table 6).

We suggest that physical and/or chemical alterations of dark spot materials are not the cause for the above temporal changes of reflectance, although for each dark spot, our significance test for the different sets of reflectance revealed substantial differences by referring to a 95% confident level (Supplementary Table 6). Photometric calibration of the MESSENGER imagery data contained residual errors of about 1.8% to 2.3% among different frames²⁶, but changes of average reflectance of dark spots are less than 3%, which are smaller than one standard deviations of the different sets of reflectance data (Supplementary Table 6). In addition, the two dark spots in the Kuiper crater exhibit enlarged reflectance in the first 15 Earth months after T0, but the reflectance suddenly decreased at the T0 + 30th month (Fig. 3c and Supplementary Table 6). It is theoretically possible that the two dark spots were decomposed or destroyed more or less

continuously in the first 15 months since T0 (i.e., enlarging the reflectance), and a sudden release of new dark spot materials between T0 + 15 month and T0 + 30 month might have occurred at both dark spots, lowering their reflectances at T0 + 30 month. However, reflectance changes of the background crater floor, where no hollows or dark spots are visible, followed exactly the same trend as that of dark spots (Fig. 3c). Our observations for another two dark spots and their background terrains yielded similar temporal changes of reflectance in 6 (Supplementary Fig. 4 and Table 7) and 18 Earth months (Supplementary Fig. 5 and Table 8), respectively. Therefore, the observed reflectance changes in both the dark spots and background terrains were unlikely caused by physical and/or chemical changes of materials in 30 Earth months, but they are more likely due to residual errors in the photometric calibration of the imagery data²⁶.

Dark spots were also imaged by the Mariner 10 spacecraft during its first (Fig. 5a) and second flyby (Supplementary Fig. 9) of Mercury at 1974, but the spatial resolution and photometric calibration³⁵ of the Mariner 10 data were not as sophisticated as those of MESSENGER data (Fig. 5). Visual comparisons of images taken by Mariner 10 and MESSENGER yield no obvious changes in the appearance of the dark spots (Fig. 5 and Supplementary Fig. 9), indicating that no substantial reflectance changes might occur in the past 40 years, at least at an observational scale of less than 730 m/pixel (Supplementary Fig. 9b).

Discussion

This study demonstrates that dark spots are a special type of LRM developed around hollows, and their reflectance spectra exhibit the largest absorption feature at ca. 560 nm (i.e., largest BD600 value) among mercurian materials. The assignment of this spectral feature to graphite could explain the low reflectance of the dark spots. Referring to the empirical relationship between BD600 value and graphite content in LRM²⁹, dark spots may contain an excess of up to 5 wt% of graphite than the global average, the highest concentration on Mercury. A potential high content of graphite in dark spots is also consistent with their extremely young stratigraphic ages, as dark spots exhibit smaller reflectances and larger BD600 values than typical LRM (Fig. 2), possibly attributable to less space weathering that would decrease the amount of graphite with time¹².

Alternatively, possible sulfides that might exist on Mercury, such as MgS and CaS as deduced from the spatial correlations of element abundances mapped by MESSENGER⁴, were invoked to explain both the absorption feature at ca. 600 nm²⁴ and/or the major hollowing-forming volatiles²¹. However, laboratory simulations revealed that such sulfides and their mixtures with analog mercurian materials were highly unstable in the day temperature of Mercury (up to 430 °C), and rapid reflectance changes within tens of minutes would occur after being heated to the day temperature of Mercury due to thermal decomposition^{20,36}. In contrast, our observations reveal no significant reflectance changes of dark spots in about 30 Earth months (i.e., about 15 Mercury days; Fig. 4), possibly up to over 40 Earth years (about 247 Mercury days; Fig. 5 and Supplementary Fig. 9). Therefore, unstable sulfides on Mercury (e.g., MgS and CaS) are unlikely to be a major component in dark spots to explain their absorption feature at ca. 560 nm, consistent with the much higher reflectances of these sulfides than those of various mercurian materials¹². The stability of chlorides such as NaCl and CaCl₂³⁷ in the hash surface environment of Mercury is unknown, but their reflectances are much higher than those of dark spots¹⁹, thus one or more opaque phases are still needed to account for their low reflectances¹⁹.

Following the current consensus that graphite may be the major darkening phase in LRM, our observations suggest that

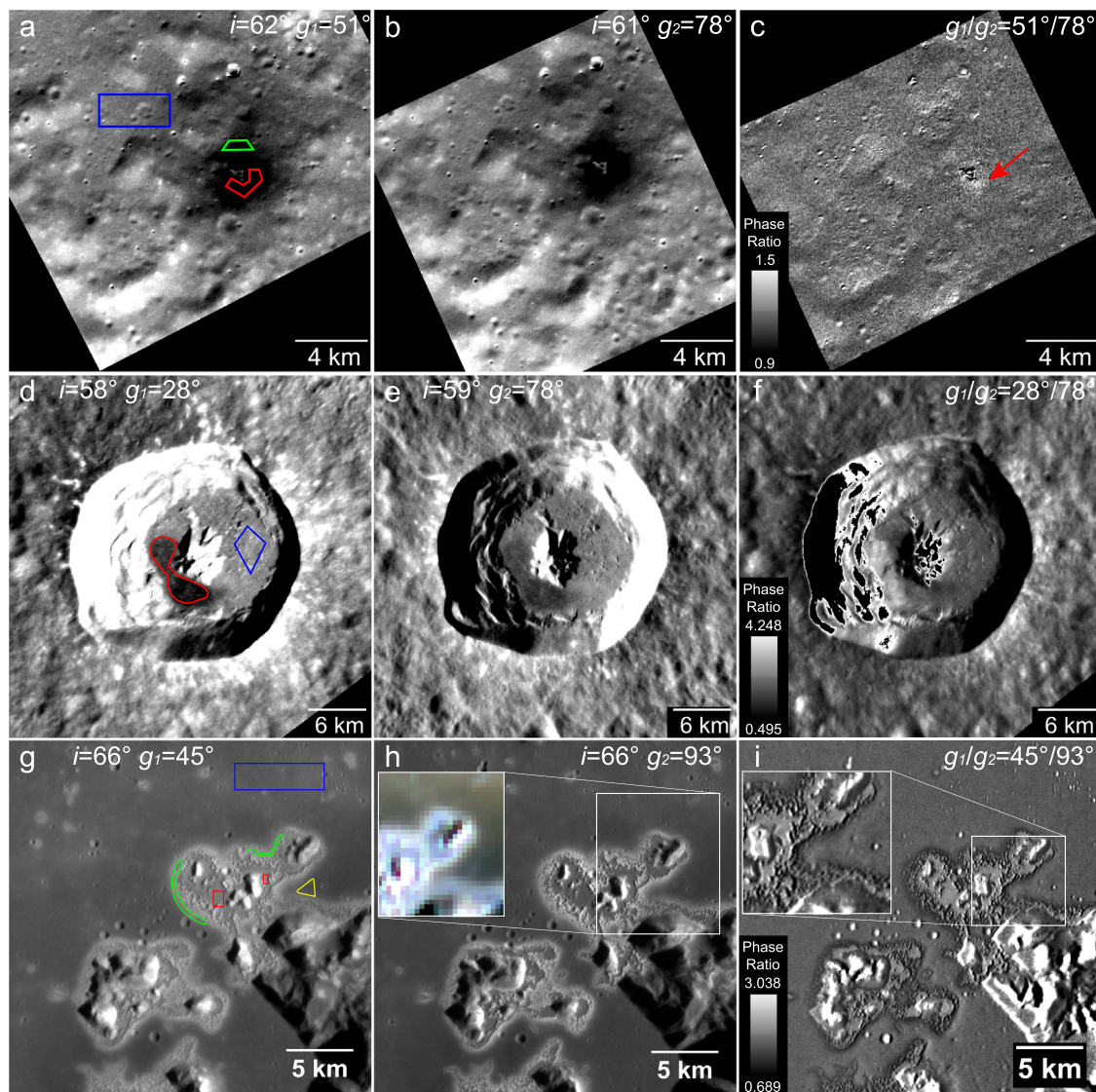


Fig. 3 Qualitative comparison of sub-pixel roughness between dark spot and regolith. For flat areas shown in the ratio map, higher values correspond to greater roughness. Left column and middle column are base images with similar incidence angles (i) and different phase angles (g). Right column are phase-ratio maps in the form of $R(g_1)/R(g_2)$ ($g_1 < g_2$) for the two base images. Black regions represent areas without ratio values. **a–c** A dark spot located at 119.754°E , 58.345°N . Red and green polygons are the regions of interest (i.e., ROI) for the inner and outer dark spots, respectively. Blue polygon is the ROI of regolith. **d–f** A dark spot located in XiaoZhao crater (236.2°E , 10.6°N). Red and blue polygons are the ROI of dark spot and regolith, respectively. **g–i** Dark spots and hollows in Eminescu crater (114.3°E , 10.7°N). Red, green, yellow, and blue polygons are the ROIs of hollow floor, bright halos, dark spots, and regolith, respectively. Subpanel in **h** is a 3-band Wide Angle Camera (WAC) image, showing the location of dark spots. The subpanel in **i** shows a detail view for the phase-ratio behavior of dark spots, which exhibit whitish tones. Base images used in all the panels are listed in the Supplementary Table 2 and provided by NASA.

reflectance changes of LRM caused by alteration of graphite due to space weathering may occur at invisible speeds to MESSENGER cameras. This result is in line with the recent observation that Mercury surface materials generally exhibit no substantial changes during the operation of the MESSENGER mission³⁸. Constrained by the average depth and maximum absolute model age of hollows, the equivalent vertical growth rate of hollows is larger than $230\ \mu\text{m}$ per Earth year, i.e., on average, depths of hollows enlarge by over $600\ \mu\text{m}$ after about 30 Earth months, or about 1 cm after 40 Earth years¹⁵. Reduction of graphite to methane by the implantation of solar wind H^+ ¹⁴ was proposed as a possible mechanism for the growth of hollows¹⁵, which may also occur in dark spot materials considering the enrichment of graphite. If destruction rate of dark spots was comparable with the annual vertical growth rate of hollows, changes of optical

properties should be anticipated when viewing at sufficient pixel and spectral resolutions after over 30 Earth months, especially at the diffuse margins where dark spot thicknesses approach optical depths¹⁵. Therefore, our observations here implicate that hollow formation may occur with a non-uniform rate (e.g., a sequence of fast initiation on formation²⁴, steady sublimation¹⁴, and episodic wall collapses¹⁵), and/or reduction of graphite in dark spots may be less efficient than that during hollow growth. Preliminary simulations for micrometeorite bombardments on graphite and its mixtures with other analog mercurian materials formed various carbon phases due to melting and/or vaporization, such as submicroscopic graphite, amorphous graphite and/or nanodiamond^{39–41}. However, the resulted reflectance changes at visible to near-infrared wavelengths were not non-uniform, which were strongly affected by the composition of the mixed analog

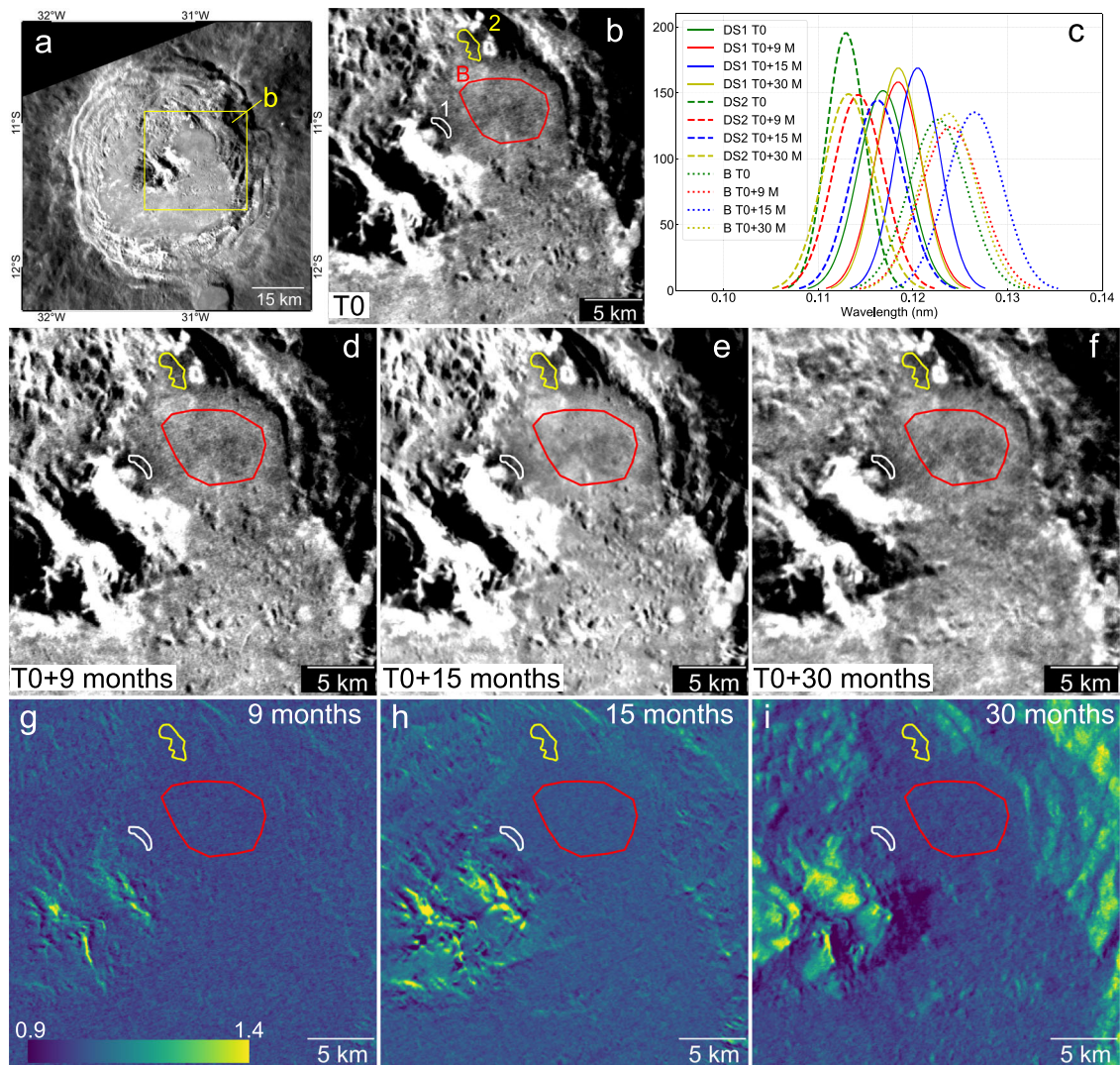


Fig. 4 No detectable changes of reflectances of dark spots on the crater floor of Kuiper in 30 Earth months. **a** Geological context of this observation. **b** Two dark spots (labeled as 1 and 2) developed along the border of the crater floor and central peak (white polygon), and crater floor and crater wall (yellow polygon). A flat and featureless crater floor (red polygon) was selected for comparison. **c** Statistics for reflectances at the 750 nm wavelength at different times of the three polygonal regions. **d-f** Co-registered images obtained 9, 15, and 30 Earth months after the acquisition of the data shown in panel **b**. **g-i** Reflectance ratios obtained by dividing the after images **d**, **e**, **f** by the before image **b**. All images are in the same stretch from 0.9 to 1.4. The control networks for this region are shown in Supplementary Fig. 6. Base images used in all the panels **a-f** are listed in the Supplementary Table 2 and provided by NASA.

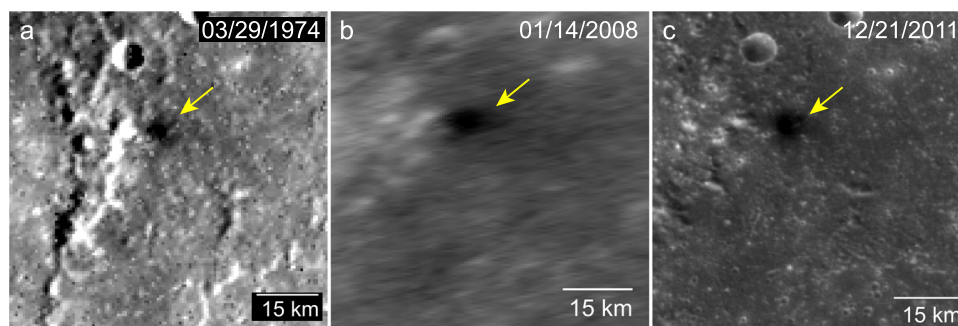


Fig. 5 Non-detectable reflectance changes of one dark spot (200 °E, 26 °N; yellow arrow) in more than 40 Earth years. **a** Mariner 10 image (mve_043_025; 664 m/pixel) acquired at 03/29/1974. **b** MDIS NAC Image (EN0108828493M; 547 m/pixel) acquired by MESSENGER during the Mercury flyby at 01/14/2008. **c** MDIS WAC Image (EW0232711987G; 321 m/pixel) acquired by MESSENGER during the orbital operation at 12/21/2011. The images were taken with similar pixel scales and incidence angles. The images are provided by NASA.

materials (e.g., quartz and iron-poor olivine)⁴¹. The absence of obvious reflectance changes of dark spots in up to about 247 Mercury days can be served as a witness plate for simulating space weathering of graphite on Mercury.

Our phase-ratio analyses lend support to an energetic outgassing origin of dark spots, suggesting that if dark spot materials have a high content of graphite, gas pressurization in the subsurface may be accompanied by incomplete volatilization of graphite and/or the outgassing event might have entrained graphite-rich materials. However, we are still impeded by two theoretical difficulties before concluding a reasonable explanation for possible mechanisms of accumulating substantial gas in the subsurface. The hypothesized outgassing events that formed dark spots might be triggered by overpressure and/or surface disturbances (e.g., sub-pixel scale impact cratering, seismic activity) of pressurized gas in the subsurface²⁴. However, current understanding suggested that once hollow formation was initiated, continual loss of volatiles likely occurred via slow processes (e.g., sublimation, decomposition) that were less energetic than regolith formation³³. For large bright-haloed hollows that have flat floors, continual volatile loss may mainly occur along steep hollow walls at the pitted halo region, and enlargement of hollows may be accomplished via wall collapse and scarp retreat that were caused by mechanical destabilization of devolatilized materials¹⁵. On the contrary, formation of dark spots by energetic outgassing requires substantial gas accumulation in the subsurface to support outburst velocities of $>100 \text{ m s}^{-1}$ ²⁴. Gas accumulation in the subsurface should be less affected by the hash surface environment. For example, transformation of graphite to methane caused by solar wind bombardment¹⁴, which was proposed as a likely mechanism of hollowing growth¹⁵, should be ineffective in the subsurface. Furthermore, hollows on Mercury have an average rim-to-floor depth of $24 \pm 16 \text{ m}$ ¹⁴, slightly less than the average thickness of regolith (25–40 m) in smooth plains⁴². If the subsurface gas body that formed dark spots was accumulated at depths shallower than the depth of hollows, the pressurized gas body would have to be within or slight below the regolith layer. However, this is difficult to reconcile, considering that the typical regolith on airless bodies such as the Moon has a large porosity⁴³.

We note that outgassing from the lunar interior was considered as a major source of certain volatile species (e.g., Ne and Ar) in the lunar exosphere⁴⁴. Recent intensive outgassing was once proposed to have dispersed mature surface regolith around the outlet, forming the apparently young irregularly shaped mare patch, Ina structure⁴⁵ that has similarly shallow floors with hollows on Mercury¹¹. However, the outgassing scenario of Ina is no longer supported by geological observations (e.g., ref. 46). Could recent intensive outgassing from the volatile-rich interior of Mercury disperse subsurface LRM, forming dark spots around the outlets (i.e., embryonic hollows in dark spots)? This possibility could explain current observations from various aspects, but the plausibility remains to be evaluated. We anticipate that the currently cruising BepiColombo spacecraft in space⁴⁷, in particular the onboard MErcury Radiometer and Thermal Imaging Spectrometer (MERTIS⁴⁸) and Spectrometer and Imaging for MPO BepiColombo Integrated Observatory SYStem (SIMBIO-SYS⁴⁹), which will be inserted into the orbit about Mercury in 2025, would return a new generation of science data that could improve our understanding of dark spots.

Methods

Base data and preprocessing. We used both single frames and various global products²⁶ of images obtained by the Mercury Dual Imaging System (MDIS) onboard MESSENGER⁵⁰, which consisted of a single-band Narrow Angle Camera (NAC) with a central wavelength of 750 nm and a Wide Angle Camera (WAC) with 11 narrow-band filters centered near 430–1020 nm. The widths of these

spectral channels are listed in the Table 2 in ref. 12. The MDIS WAC eight-band global color mosaic (665 m/pixel) has a minimum residual error of ca. 2% in photometric calibration for most Mercury surfaces, and this dataset is suitable for quantitative comparison of spectral heterogeneities across the globe²⁶. Therefore, we extracted reflectance spectra for dark spots and other terrains using this global dataset instead of regional multi-band WAC mosaics. Single-frame MDIS images were used for targeted observations. The USGS Integrated Software for Imagers and Spectrometers (ISIS; <https://isis.astrogeology.usgs.gov>) was used to calibrate and process single-frame MDIS data following the standard pipeline²⁶. The Kaasalainen-Shkuratov model^{51,52} (K-S model) was used for photometric calibration²⁶. Supplementary Table 2 lists the IDs of data used in this study.

Updating the global inventory of dark spots. We applied the same definition of dark spots that was proposed earlier when updating the global inventory, i.e., dark spots are spatially isolated dark and diffuse materials developed around hollows, and they were not obviously formed by impact cratering or volcanic eruption²⁴. High-resolution NAC and multi-bands WAC images obtained during the entire mission of MESSENGER were used for global investigation of dark spots. The global database of dark spots is presented in the Supplementary Table 1.

Relationship between LRM and dark spots. While dark spots were only observed in materials that have lower reflectances than high-reflectance red plains²⁴, the relationship between LRM and dark spot materials was not evaluated. LRM is defined by their unique spectral properties²⁹: a photometrically corrected reflectance of <0.0565 at 560 nm wavelength, a second principal component of less than 0.0375, and a spectral slope of 0.0515–0.0640 represented by ratios of reflectance at 430 nm and 1000 nm. We followed this spectral definition of LRM and compared the global distributions of LRM^{24,29} and dark spots. In addition, typical LRM exhibits a shallow absorption at ca. 560 nm, and the band depth here (BD600¹²) was interpreted to be positively correlated with the carbon (in the form of graphite) content^{6,29}. The value of BD600 is defined based on reflectances at central wavelength of the 550 nm, 630 nm, 750 nm, and 830 nm filter channels relative to a continuum tied to the 480 and 900 nm channels¹²:

$$\text{BD600} = 1 - \left[\frac{(R_{560} + R_{630} + R_{750} + R_{830})/4}{(R_{900} + R_{480})/2} \right]$$

where R is photometrically corrected reflectance in each of the given filters. Considering that some recently discovered darkish pyroclastic deposits on Mercury exhibit negative absorption at ca. 600 nm (i.e., $\text{BD600} < 0$; ref. 18), we also used the BD600 values of dark spots to evaluate the relative concentration of graphite. The global distribution of LRM and global map of BD600 are both derived based on the MDIS eight-band global color mosaics, and are available at <https://doi.org/10.5281/zenodo.5788575>⁵³.

Reflectance spectra of dark spots and other mercurian materials. We compared the reflectance spectra of dark spots, flat hollow floors¹⁵, LRM⁵⁴, and LBP⁵⁴. To ensure that the sampled pixels for dark spots avoided shadows, background materials (e.g., margins of dark spots), and nearby heterogeneous materials (e.g., ejecta rays, bright halos of hollow, pyroclastic deposits), we performed manual georeferencing for high-resolution MDIS images over the global eight-band color mosaic. For each dark spot target (Supplementary Fig. 2), we extracted their reflectance spectra using sampled pixels that were entirely located within the dark spots as seen in georeferenced high-resolution images.

Analyses of phase-ratio behaviors of dark spots to detect sub-pixel roughness. Reflectances of planetary surface materials change at various rates as the observational phase angles (i.e., the angle between the directions of incidence and emergence) change⁵⁵. This phenomenon can be used to infer differences in particle sizes or sub-pixel texture of the surface materials³². For dark spots that have multiple coverages of suitable NAC images for phase-ratio analyses³² (i.e., similar pixel scales, incidence angles, and more than 20° difference of phase angles), we compared the semi-qualitative sub-pixel roughness for dark spots, other hollow facies, and background regolith. Phase-ratio images are obtained by dividing larger-phase-angle reflectances over smaller-phase-angle reflectances based on co-registered MDIS images.

Analyses of temporal images of dark spots to detect possible changes of reflectances. To detect potential changes of dark spots, we used the temporal imaging technique (e.g., ref. 56) for cases that were covered by suitable temporal NAC images, i.e., similar pixel resolutions, incidence angles, emission angles, azimuth, but different acquisition times. Before comparing the before- and after-images, we performed high-precision registration for the temporal images using the coreg module in ISIS. The registration accuracy for areas that have imperfect automatic registration by coreg was further improved by adding manually added control points.

Data availability

MDIS NAC and WAC datasets are available in ref. 57. MDIS global color mosaics are available on <http://messenger.jhuapl.edu/Explore/Images.html#global-mosaics>. The global LRM distribution map and BD600 map is available in the online repository (<https://doi.org/10.5281/zenodo.5788575>)⁵³. The updated inventory of dark spots (i.e., Supplementary Table 1) is available in the online repository (<https://doi.org/10.5281/zenodo.7055841>)⁵⁸. The IDs of MDIS images used in this study are listed in the Supplementary Table 2.

Received: 21 June 2022; Accepted: 17 November 2022;

Published online: 29 November 2022

References

- McCoy, T. J. et al. In *Mercury: The view after MESSENGER* (eds. Solomon, S. C., Nittler, L. R. & Anderson, B. J.) 176–190 (Cambridge Univ. Press, 2018).
- Evans, L. G. et al. Major-element abundances on the surface of Mercury: results from the MESSENGER gamma-ray spectrometer. *J. Geophys. Res.* **117**, E00L07 (2012).
- Nittler, L. R. et al. The major-element composition of Mercury's surface from MESSENGER X-ray Spectrometry. *Science* **333**, 1847–1850 (2011).
- Weider, S. Z. et al. Evidence for geochemical terranes on Mercury: The first global mapping of major elements on the surface of the innermost planet. *Earth Planet. Sci. Lett.* **416**, 109–120 (2015).
- Peplowski, P. N. et al. Constraints on the abundance of carbon in near-surface materials on Mercury: results from the MESSENGER Gamma-Ray Spectrometer. *Planet. Space Sci.* **108**, 98–107 (2015).
- Peplowski, P. N. et al. Remote sensing evidence for an ancient carbon-bearing crust on Mercury. *Nat. Geosci.* **9**, 273–276 (2016).
- Evans, L. G. et al. Chlorine on the surface of Mercury: MESSENGER gamma-ray measurements and implications for the planet's formation and evolution. *Icarus* **257**, 417–427 (2015).
- Zolotov, M. Y. et al. The redox state, FeO content, and origin of sulfur-rich magmas on Mercury. *J. Geophys. Res. Planets* **118**, 138–146 (2013).
- Clement, M. S. et al. Mercury as the relic of Earth and Venus outward migration. *Astrophys. J. Lett.* **923**, L16 (2021).
- Kerber, L. et al. Explosive volcanic eruptions on Mercury: eruption conditions, magma volatile content, and implications for interior volatile abundances. *Earth Planet. Sci. Lett.* **285**, 263–271 (2009).
- Blewett, D. T. et al. Hollows on Mercury: MESSENGER evidence for geologically recent volatile-related activity. *Science* **333**, 1856–1859 (2011).
- Murchie, S. L. et al. Orbital multispectral mapping of Mercury with the MESSENGER Mercury Dual Imaging System: evidence for the origins of plains units and low-reflectance material. *Icarus* **254**, 287–305 (2015).
- Vander Kaaden, K. E. & McCubbin, F. M. Exotic crust formation on Mercury: consequences of a shallow, FeO-poor mantle. *J. Geophys. Res. Planets* **120**, 195–209 (2015).
- Blewett, D. T. et al. Analysis of MESSENGER high-resolution images of Mercury's hollows and implications for hollow formation. *J. Geophys. Res. Planets* **121**, 1798–1813 (2016).
- Wang, Y., Xiao, Z., Chang, Y. & Cui, J. Lost volatiles during the formation of hollows on Mercury. *J. Geophys. Res. Planets* **125**, e2020JE006559 (2020).
- Weider, S. Z. et al. Evidence from MESSENGER for sulfur- and carbon-driven explosive volcanism on Mercury. *Geophys. Res. Lett.* **43**, 3653–3661 (2016).
- Li, Y., Dasgupta, R. & Tsuno, K. Carbon contents in reduced basalts at graphite saturation: Implications for the degassing of Mars, Mercury, and the Moon. *J. Geophys. Res. Planets* **122**, 1300–1320 (2017).
- Xiao, Z. et al. Recent dark pyroclastic deposits on Mercury. *Geophys. Res. Lett.* **48**, e2021GL092532 (2021).
- Lucchetti, A. et al. Volatiles on Mercury: the case of hollows and the pyroclastic vent of Tyagaraja crater. *Icarus* **370**, 114694 (2021).
- Helbert, J., Maturilli, A. & D'Amore, M. Visible and near-infrared reflectance spectra of thermally processed synthetic sulfides as a potential analog for the hollow forming materials on Mercury. *Earth Planet. Sci. Lett.* **369–370**, 233–238 (2013).
- Vilas, F. et al. Mineralogical indicators of Mercury's hollows composition in MESSENGER color observations. *Geophys. Res. Lett.* **43**, 1450–1456 (2016).
- Philips, M. S., Moersch, J. E., Viviano, C. E. & Emery, J. P. The lifecycle of hollows on Mercury: an evaluation of candidate volatile phases and a novel model of formation. *Icarus* **359**, 114306 (2021).
- Blewett, D. T. et al. Mercury's hollows: constraints on formation and composition from analysis of geological setting and spectral reflectance. *J. Geophys. Res. Planets* **118**, 1013–1032 (2013).
- Xiao, Z. et al. Dark spots on Mercury: a distinctive low-reflectance material and its relation to hollows. *J. Geophys. Res. Planets* **118**, 1752–1765 (2013).
- Solomon, S. C. et al. MESSENGER mission overview. *Space Sci. Rev.* **131**, 3–39 (2007).
- Denevi, B. W. et al. Calibration, projection, and final image products of MESSENGER's Mercury Dual Imaging System. *Space Sci. Rev.* **214**, 52 (2018).
- Soter, S. & Ulrichs, J. Rotation and heating of the planet Mercury. *Nature* **214**, 1315–1316 (1967).
- Denevi, B. W. et al. The evolution of Mercury's crust: a global perspective from MESSENGER. *Science* **324**, 613–618 (2009).
- Klima, R. L., Denevi, B. W., Ernst, C. M., Murchie, S. L. & Peplowski, P. N. Global distribution and spectral properties of low-reflectance material on Mercury. *Geophys. Res. Lett.* **45**, 2945–2953 (2018).
- Lucchetti, A. et al. Mercury hollows as remnants of original bedrock materials and devolatilization processes: a spectral clustering and geomorphological analysis. *J. Geophys. Res. Planets* **123**, 2365–2379 (2018).
- Cloutis, E. A. Pyroxene reflectance spectra: miner absorption bands and effects of elemental substitutions. *J. Geophys. Res.* **107**, 5039 (2002).
- Kaydash, V., Shkuratov, Y. & Videen, G. Phase-ratio imagery as a planetary remote-sensing tool. *J. Quant. Spectrosc. Radiat. Transf.* **113**, 2601–2607 (2012).
- Blewett, D. T. et al. Phase-ratio images of the surface of Mercury: evidence for differences in sub-resolution texture. *Icarus* **242**, 142–148 (2014).
- Banks, M. E. et al. Revised constraints on absolute age limits for Mercury's Kuiperian and Mansurian stratigraphic system. *J. Geophys. Res. Planets* **122**, 1010–1020 (2017).
- Robinson, M. S. & Lucey, P. G. Recalibrated Mariner 10 color mosaics: implications for Mercurian volcanism. *Science* **275**, 197–200 (1997).
- Serventi, G. et al. *Emissivity and Reflectance Spectra of Sulfide-bearing Samples: New Constraints for the Hermean Surface Composition* (European Planetary Science Congress, EPSC2018-92-1, 2018).
- Carroll, M. R. & Webster, J. D. Solubilities of sulfur, noble gases, nitrogen, chlorine, and fluorine in magmas. *Rev. Mineral. Geochem.* **30**, 231–279 (1994).
- Speyerer, E. J., Robinson, M. S. & Snoko, A. J. Present day endogenic and exogenic activity on Mercury. *Geophys. Res. Lett.* **49**, e2022GL100783 (2022).
- Bruck Syal, M. et al. Darkening of Mercury's surface by cometary carbon. *Nat. Geosci.* **8**, 3653–3661 (2015).
- Trang, D. et al. Space weathering of graphite: application to Mercury. *49th Lunar and Planetary Science Conference, Houston*. Abstract #2083 (2018).
- Thompson, M. S. et al. Understanding the space weathering of Mercury through laboratory experiments. *52nd Lunar and Planetary Science Conference, Houston*. Abstract #2548 (2021).
- Kreslavsky, M. A. & Head, J. W. A thicker regolith on Mercury. *Lunar and Planetary Science Conference, Houston*. Abstract #1832 (2015).
- Heiken, G. H., Vaniman, D. T. & French, B. M. *Lunar Sourcebook, A User's Guide to the Moon*. 1–753 (Cambridge Univ. Press, New York, 1991).
- Hodges, R. R. Release of radiogenic gases from the moon. *Phys. Earth Planet. Interior.* **14**, 282–288 (1977).
- Schultz, P. H., Staid, M. I. & Pieters, C. M. Lunar activity from recent gas release. *Nature* **444**, 184–186 (2006).
- Braden, S. E. et al. Evidence for basaltic volcanism on the Moon within the past 100 million years. *Nat. Geosci.* **7**, 787–791 (2014).
- Benkhoff, J. et al. BepiColombo—comprehensive exploration of Mercury: mission overview and science goals. *Planet. Space Sci.* **58**, 2–20 (2010).
- Hiesinger, H. et al. Studying the composition and mineralogy of the hermean surface with the Mercury Radiometer and Thermal Infrared Spectrometer (MERTIS) for the BepiColombo Mission: an update. *Space Sci. Rev.* **216**, 110 (2020).
- Cremonese, G. et al. SIMBIO-SYS: Scientific cameras and spectrometer for the BepiColombo mission. *Space Sci. Rev.* **216**, 75 (2020).
- Hawkins, S. E. et al. The mercury dual imaging system on the MESSENGER spacecraft. *Space Sci. Rev.* **131**, 247–338 (2007).
- Kaasalainen, M., Torppa, J. & Muinonen, K. Optimization methods for asteroid lightcurve inversion. *Icarus* **153**, 37–51 (2001).
- Shkuratov, Y. et al. Optical measurements of the Moon as a tool to study its surface. *Planet. Space Sci.* **59**, 1326–1371 (2011).
- Xu, R. Less than half weight percent of graphite on the surface of Mercury. <https://doi.org/10.5281/zenodo.5788575> (2022).
- Murchie, S. L. et al. in *Mercury: The view after MESSENGER* (eds. Solomon, S. C., Nittler, L. R. & Anderson, B. J.) 191–216 (Cambridge University of Press, 2018).
- Hapke, B. *Theory of reflectance and emittance spectroscopy* (Cambridge Univ. Press, 2012).
- Speyerer, E. J., Povilaitis, R. Z., Robinson, M. S., Thomas, P. C. & Wagner, R. V. Quantifying crater production and regolith overturn on the Moon with temporal imaging. *Nature* **538**, 215–218 (2016).
- Hash, C. D. *Messenger MDIS Experiment Data Record V1.0*. NASA Planetary Data System. <https://doi.org/10.17189/1520380> (2015).

58. Wang, Y. Non-detected changes of dark spots on Mercury in 30 Earth months. <https://doi.org/10.5281/zenodo.7055841> (2022).

Acknowledgements

The authors are grateful to the editors and reviewers for their helpful review. This research is supported by the National Natural Science Foundation of China (42273040, 41773063), the B-type Strategic Priority Program of the Chinese Academy of Sciences (grant XDB41000000), and China Manned Space Engineering Program.

Author contributions

Y.W.: investigation, methodology, formal analyses, data curation, visualization and writing. Zhiyong X.: conceptualization, methodology, formal analyses, data curation, writing and funding acquisition. R.X.: generated global spectral maps. Zhouxuan X.: contributed high-precision registration for the temporal images. J.C.: funding acquisition. All the authors contributed to discussions and revision.

Competing interests

The authors declare no competing interests.

Additional information

Supplementary information The online version contains supplementary material available at <https://doi.org/10.1038/s43247-022-00634-z>.

Correspondence and requests for materials should be addressed to Zhiyong Xiao.

Reprints and permission information is available at <http://www.nature.com/reprints>

Publisher's note Springer Nature remains neutral with regard to jurisdictional claims in published maps and institutional affiliations.



Open Access This article is licensed under a Creative Commons Attribution 4.0 International License, which permits use, sharing, adaptation, distribution and reproduction in any medium or format, as long as you give appropriate credit to the original author(s) and the source, provide a link to the Creative Commons license, and indicate if changes were made. The images or other third party material in this article are included in the article's Creative Commons license, unless indicated otherwise in a credit line to the material. If material is not included in the article's Creative Commons license and your intended use is not permitted by statutory regulation or exceeds the permitted use, you will need to obtain permission directly from the copyright holder. To view a copy of this license, visit <http://creativecommons.org/licenses/by/4.0/>.

© The Author(s) 2022